Nano Research

Open Access

Research Article

Unveiling the superior hydrogen evolution reaction activity of 1T-2H MoS_2 heterointerface by on-chip microdevices

Bowen Liu[1,2,§], Junjie Xiong[1,2,§], Shuaishuai Xu[1,3], Xinying Luo[1,2], Wenyan Yao[1,2], Shigang Liu[1], Yuting Du[3], Qinghua Zhang[4], Yang Gao[1,2] ✉, and Bin Wang[1,2] ✉

[1] *CAS Key Laboratory of Nanosystem and Hierarchical Fabrication, National Center for Nanoscience and Technology (NCNST), Beijing 100190, China*
[2] *University of Chinese Academy of Sciences, Beijing 100049, China*
[3] *School of Materials Science and Engineering, China University of Petroleum (East China), Qingdao 266580, China*
[4] *Beijing National Laboratory for Condensed Matter Physics, Institute of Physics, Chinese Academy of Sciences, Beijing 100190, China*
§ *Bowen Liu and Junjie Xiong contributed equally to this work.*

Cite this article: *Nano Research*, **2025**, *18*, 94907020. https://doi.org/10.26599/NR.2025.94907020

ABSTRACT: The identification and clarification of active sites of MoS_2 have long been the focus of research efforts in hydrogen evolution reaction (HER). In this study, we constructed phase transition-induced 1T-2H MoS_2 heterojunction via lithium intercalation and evaluated the HER activity using on-chip electrocatalytic microdevices (OCEMs). The heterojunction achieved an overpotential of only 226 mV at a cathodic current density of 10 mA/cm^2, outperforming the basal planes of 1T and 2H MoS_2. Furthermore, density functional theory (DFT) calculations demonstrated that the charge redistribution occurs at the 1T-2H MoS_2 interface with electrons transferring from 1T to 2H MoS_2, and the interfacial S atom at the top site of 1T MoS_2 presents the smallest overpotential of 0.37 V. Moreover, the interference from highly active edge sites was avoided by precisely exposing specific active areas, quantitatively revealing the catalytic activity order of different types of in-plane MoS_2 active sites. This work enables a systematic investigation of the HER activity of various active sites in MoS_2, laying the foundation for quantitative analysis of activity in other low-dimensional materials.

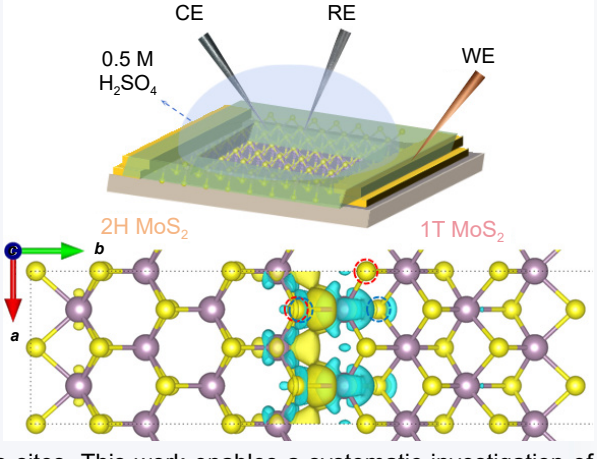

KEYWORDS: on-chip microdevice, phase transition, heterojunction, MoS_2, hydrogen evolution reaction (HER)

1 Introduction

Over the past decade, molybdenum disulfide (MoS_2) has been considered a low-cost and promising alternative to noble metal catalysts due to its rapid interfacial charge transfer and high hydrogen evolution reaction (HER) activity [1–4]. The identification and clarification of the active sites of MoS_2 have long been the focus of research efforts [5–9]. Conventional theories posit that in comparison to the chemically inert basal plane, the active sites in MoS_2 predominantly reside at Mo-terminated edges [10–12], sulfur vacancies [13–16], and grain boundaries [17, 18]. Additionally, the basal-plane HER activity can be significantly enhanced by transforming the room-temperature stable semiconductor 2H-phase MoS_2 into the metallic 1T phase [19, 20]. Therefore, extensive efforts are devoted to creating more sulfur vacancies or enriching in-plane 1T-2H heterojunctions to modulate the less active basal plane sites and enhance their HER performance [21]. However, the assessment of activity across different types of catalytic sites primarily occurs in powder materials, presenting challenges in isolating the diverse influencing factors for direct quantitative comparison of distinct active sites in MoS_2. For instance, theoretical calculations indicate that the edge sites of MoS_2 exhibit excellent catalytic activity, with the hydrogen adsorption free energy (ΔG_H) of only 0.06 eV, comparable to that of noble metal Pt [22]. However, when comparing the activity of different samples,

Received: June 26, 2024; **Revised:** August 16, 2024
Accepted: September 2, 2024

✉Address correspondence to Yang Gao, gaoyang@nanoctr.cn; Bin Wang, wangb@nanoctr.cn

the presence of numerous edge sites in powdered samples is often overlooked. Thus, the overall activity is inaccurately attributed to customized sites, preventing a genuine comparison of catalytic activities.

Recently, on-chip electrocatalytic microdevices (OCEMs) have emerged as a novel approach to achieving high-precision electrochemical measurements of individual nanomaterials at the microscale, providing a unique perspective inaccessible to traditional electrochemical methods [23–29]. In this study, for the first time, a well-defined long-range ordered 1T-2H MoS_2 heterojunction with a smooth surface was synthesized via lithium intercalation, thus serving as a model catalyst and eliminating the influence of edges, wrinkles, and substrates. Subsequently, its HER activity was studied by OCEMs constructed by micro-/nanofabrication techniques. Experimental results demonstrate that the 1T-2H MoS_2 heterojunction exhibits significantly enhanced in-plane HER activity, with an overpotential of 226 mV at a cathodic current density of 10 mA/cm^2. Furthermore, density functional theory (DFT) calculations indicate that the charge redistribution occurs at the 1T-2H MoS_2 interface with electrons transferring from 1T to 2H MoS_2, leading to a decreased HER energy barrier. This study systematically explored the HER activity of various in-plane active sites in MoS_2 by electrocatalytic tests at the microregion level, establishing a fundamental basis for quantitatively analyzing activity in low-dimensional materials.

2 Results and discussion

Layered transition metal dichalcogenides (TMDs) can be efficiently exfoliated via lithium intercalation and subsequent addition of excess water which leads to hydrogen formation and forced separation of the layers [30, 31]. In the case of MoS_2, electron transfer from Li during intercalation causes a change in the electron count from d^2 to d^3, leading to the destabilization of the original crystal structure. Specifically, Li intercalation results in a change in the metal coordination from trigonal prismatic (2H) to octahedral geometry (1T) [32].

The schematic diagram and atomic structure of partial lithiation-induced phase transition are shown in Fig. 1(a). By controlling the lithiation time and extent of the reaction appropriately, partial lithiation of the 2H MoS_2 can be achieved, thereby enabling the coexistence of 1T and 2H phases within the planar heterojunction. Figures 1(b) and 1(c) show the optical images of MoS_2 before and after partial lithiation, demonstrating that the lithiation of MoS_2 proceeded gradually from the edges of the layers towards the interior. Consequently, a distinct boundary between the 1T and 2H phases was formed. The changes in the lattice parameters of partially lithiated MoS_2 were characterized by transmission electron microscopy (TEM). As shown in Fig. 1(d), distinct contrast boundaries indicate the formation of lithiated regions. High-resolution TEM (HRTEM) images (Figs. 1(e) and 1(g)) show the in-plane trigonal 2H phase and octahedral 1T phase of MoS_2 with their corresponding fast Fourier transforms (inset). Additionally, the (002) crystal planes of lithiated regions exhibit an expanded interlayer spacing of 0.63 nm compared to the unlithiated spacing of 0.61 nm (Figs. 1(f) and 1(h)). The increase in interlayer spacing caused by lithium intercalation was further characterized by X-ray diffraction (XRD). As shown in Fig. S1 in the Electronic Supplementary Material (ESM), all peaks of 1T MoS_2 shifted to a lower degree compared to pristine 2H MoS_2, with the 2θ of (002) peak decreasing from 14.5° to 14.0°, which is consistent with the HRTEM results [33]. Energy dispersive X-ray spectrometry (EDS) results demonstrate that lithiation does not affect the uniform distribution of Mo and S elements (Fig. S2 in the ESM). Additionally, as shown in Fig. S3 in the ESM, the MoS_2 basal plane exhibits a relatively intact planar structure both before and after the phase transition, further confirming the uniformity of the phase transition. Furthermore, aberration corrected high angle annular dark field-scanning transmission electron microscopy (AC-HAADF-STEM) was applied for a detailed observation of the in-plane atomic arrangement of 1T-2H MoS_2. As shown in Fig. 1(i), the planes with a lattice spacing of 0.27 nm in 2H MoS_2 correspond to the (100) planes, whereas in the 1T phase, the same plane spacing is typically identified as the (101) plane. The red dashed line indicates the well-defined long-range ordered in-plane 1T-2H heterojunction. For a clearer comprehension, the schematic atomic arrangements of the 1T and 2H phases are presented in Figs. 1(j) and 1(k), respectively, which align well with the intensity profiles of the dashed box (Figs. 1(l) and 1(m)). Due to the overlap of two S atoms along the electron beam direction between adjacent Mo atoms in the 2H phase, there is a relative signal enhancement of lattice points compared to the 1T phase, where sulfur atoms are separated.

Raman spectroscopy was collected to identify the chemical state of lithiated MoS_2. Figure 2(a) illustrates the Raman mapping image of the partially lithiated MoS_2 at 156 cm^{-1}. For 2H-MoS_2 (Fig. 2(b)), the characteristic peaks attributed to E^1_{2g} and A_{1g} are located at 383.4 and 407.9 cm^{-1}, respectively, indicating that Region 2 remains unlithiated. In contrast, in Region 1, the disappearance of the E^1_{2g} peak is accompanied by the emergence of three additional vibration peaks, J_1 (153 cm^{-1}), J_2 (221 cm^{-1}), and J_3 (331 cm^{-1}), indicative of the 1T-phase MoS_2 [34]. Figure 2(c) shows an integrated PL intensity mapping of the partially lithiated MoS_2. The PL intensity of the lithiated region was found to be much smaller than that of the unlithiated region, suggesting that the charge recombination of the lithiated region was more efficiently inhibited quenching because of the presence of the 1T phase (Fig. 2(d)).

Furthermore, X-ray photoelectron spectroscopy (XPS) was applied to explore the phase composition and valence states of MoS_2 (Fig. S4 in the ESM). As given in Fig. 2(e), for the pristine 2H MoS_2 nanosheets, most of the Mo signal arises from a $3d_{5/2}$ peak at 229.6 eV and a $3d_{3/2}$ peak at 232.3 eV, both of which are characteristic of the Mo^{4+} oxidation state. In comparison, for the 1T-2H MoS_2, the two peaks can be deconvoluted into two sets of characteristic peaks where the two peaks at 229.3 and 232.1 eV are assigned to Mo^{4+} $3d_{5/2}$ and $3d_{3/2}$ of 2H MoS_2, respectively, while the other two peaks at 227.6 and 230.1 eV correspond to Mo^{4+} $3d_{5/2}$ and $3d_{3/2}$ of 1T MoS_2, respectively. Besides, the peak of S 2s at 225.5 eV is attributed to the terminal S in Mo–S bonds, while the peak of Mo^{6+} at 234.2 eV suggests the presence of Mo-based oxides which were formed due to the inevitable oxidation of edge Mo in metastable 1T-phase MoS_2 under high-energy X-ray irradiation during the XPS testing process [35]. Apart from the doublet peaks of 2H MoS_2 (162.65 and 163.85 eV), the two peaks at 162.2 and 163.4 eV in the S 2p spectra correspond to the S $2p_{3/2}$ and S $2p_{1/2}$ of 1T MoS_2, respectively, further verifying the coexistence of 1T and 2H phases in the 1T-2H MoS_2 (Fig. 2(f)).

Then, the concentration of n-butyllithium and the duration of treatment were varied systematically to elucidate its impact on the phase transformation trends of MoS_2. Specifically, MoS_2 thin films of uniform thickness were treated with n-butyllithium solutions at concentrations of 1.6 M (Figs. S5(a)–S5(d) in the ESM) and 2.4 M

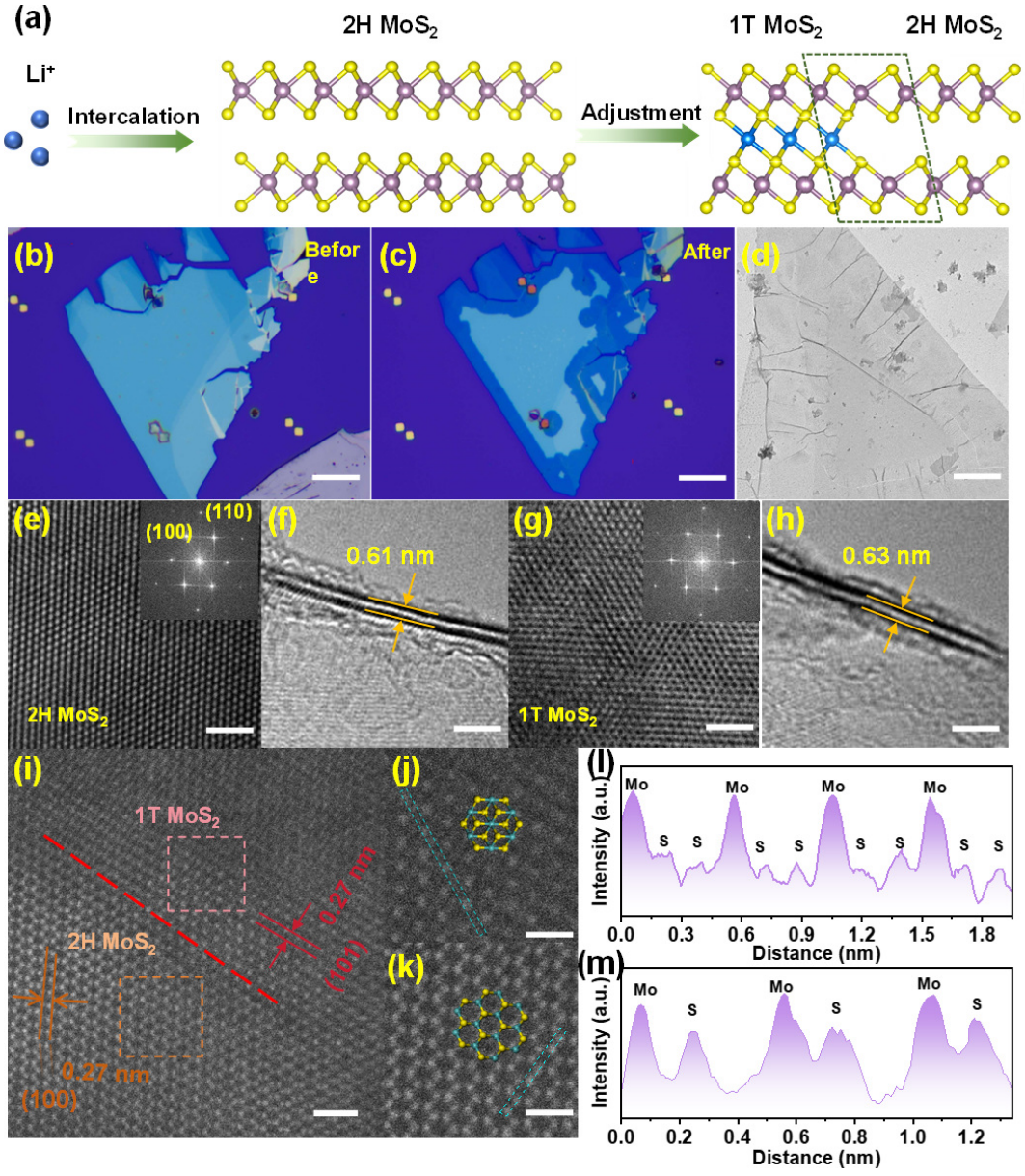

Figure 1 (a) Schematic diagram and atomic structure of the partial lithiation-induced phase transition from 2H to 1T-2H MoS_2. (b) and (c) Typical optical images of (b) 2H and (c) 1T-2H MoS_2. Scale bar: 10 μm. (d) TEM image of 1T-2H MoS_2 where the coexistence of 1T and 2H can be observed through a comparison of contrast. Scale bar: 1 μm. (e) and (g) HRTEM images of (e) 2H and (g) 1T MoS_2 with their corresponding Fourier transforms (inset). Scale bar: 2 nm. (f) and (h) HRTEM images of (f) 2H and (h) 1T MoS_2 to reveal the interlayer spacing of (002) crystal planes. Scale bar: 2 nm. (i) HAADF-STEM image of 1T-2H MoS_2. Scale bar: 1 nm. (j) and (k) Magnified images of the dashed boxes in (i) for 1T MoS_2 and 2H MoS_2 with the corresponding structural schematic inside. Scale bar: 0.5 nm. (l) and (m) Atomic arrangement profiles along the marked lines in (j) and (k).

(Figs. S5(e)–S5(h) in the ESM). The degree of phase conversion was characterized using optical microscopy and Raman spectroscopy after lithiation durations of 1, 2, and 5 h. As observed in Fig. S5 in the ESM, the degree of lithiation increases progressively with time for both concentration treatments. Notably, the treatment with a higher concentration of n-butyllithium results in a larger phase-transformed area of MoS_2 for the same treatment duration, indicating a faster lithiation rate. This can be attributed to the fact that a higher concentration of n-butyllithium can inject more electrons at the same time, thereby accelerating the phase transition. In this study, we defined the initiation of the phase conversion by the emerging of J_1 peak at 153 cm^{-1}, which is the most prominent peak of the 1T phase, and the absence of the E^1_{2g} mode at 383 cm^{-1}, which is non-Raman active in 1T phase, was taken as the sign for the complete disappearance of 2H phase. From the Raman spectra in Figs. S5(i) and S5(j) in the ESM, it can be observed that after treatment with 2.4 M n-butyllithium solution for 5 h, the E^1_{2g} mode at 383 cm^{-1} in the tested region almost completely disappears, indicating a full phase transition from 2H to 1T in the MoS_2.

To investigate the catalytic activity of different types of in-plane active sites in MoS_2, the OCEMs were fabricated to compare their HER performance. Figure S6 in the ESM depicts the integration of miniature three-electrode systems on the chip platform. As shown in Figs. S6(a) and 6(b) in the ESM, the designated windows in the prepared electrocatalytic microdevices were exposed to the 0.5 M H_2SO_4 electrolyte for HER activity testing, while other regions

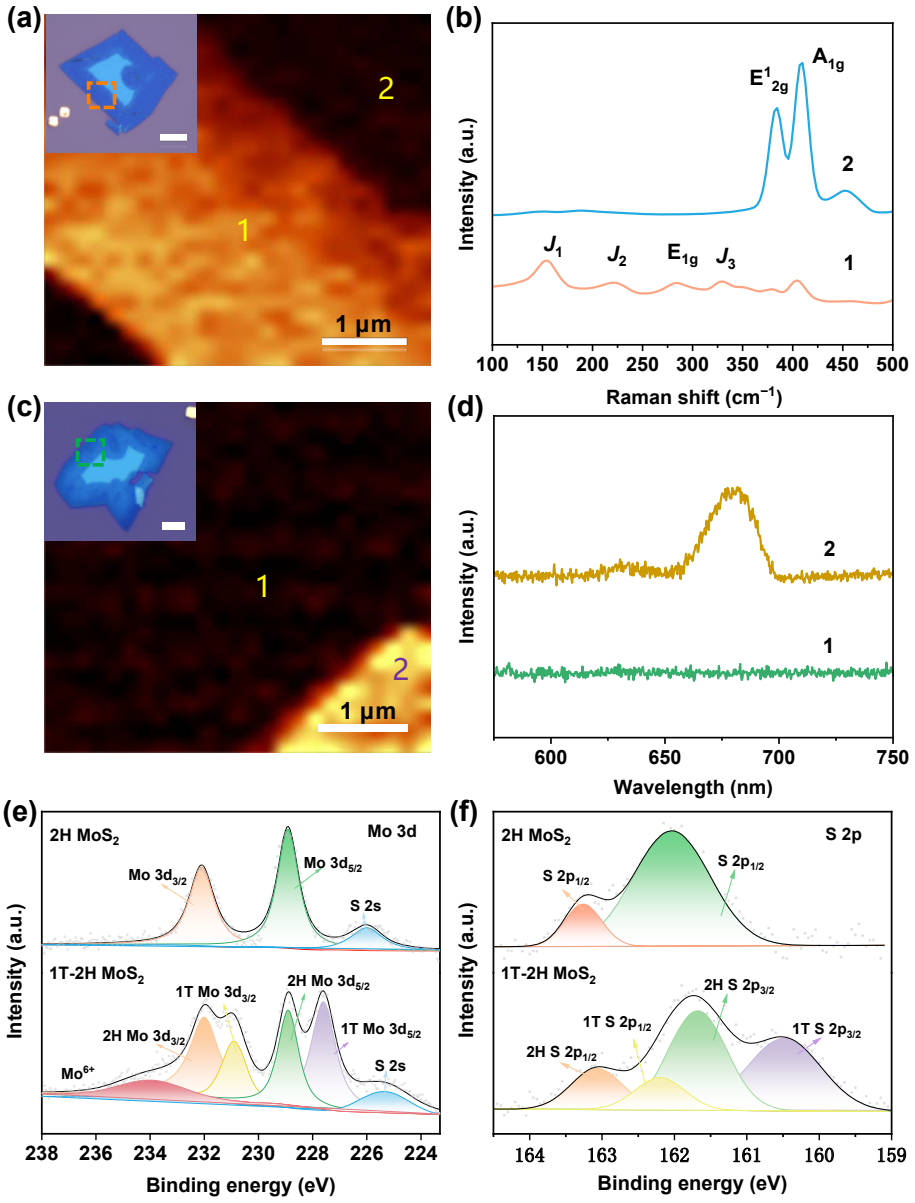

Figure 2 (a) Raman mapping image of the rectangular region marked in the inset (scale bar: 4 μm) at 156 cm^{-1}. (b) Raman spectra at the marked position in (a). (c) PL mapping image of the rectangular region marked in the inset at 675 nm. (d) PL spectra at the marked position in (c). (e) and (f) XPS spectra of Mo 3d and S 2p in 2H and 1T-2H MoS_2.

remained covered with polymethyl methacrylate (PMMA) to ensure that the measured activity originated solely from the exposed regions. Figure 3(a) compares the polarization curves of different types of in-plane MoS_2 active sites. The 1T-2H MoS_2 heterojunction exhibits the optimal HER activity, with an overpotential of only 226 mV at a cathodic current density of 10 mA/cm^2 (345 mV for 1T MoS_2 and 445 mV for 2H MoS_2). Additionally, as shown in Fig. 3(b), the Tafel slope of 1T-2H MoS_2 is about 109 mV/dec, which is much lower than that of 2H MoS_2 (149 mV/dec) and 1T MoS_2 (146 mV/dec), suggesting that the heterojunction possesses the optimal reaction kinetics for HER [36]. Additionally, the 1T-2H MoS_2 heterojunction demonstrates comparable performance when compared to other well-designed two-dimensional (2D) materials tested by on-chip microdevice (Table S1 and Fig. S7 in the ESM). Moreover, to quantitatively calculate the turnover frequency (TOF) of different in-plane sites, the density of active sites was counted based on the atomic structure of monolayer 2H-MoS_2 (Fig. S8 in the ESM). As a result, the active site density of the basal plane is determined to be $\approx 1.14 \times 10^{19}$ m^{-2}. The TOF of different MoS_2 sites were calculated according to the following equation: TOF = j_o/ncz, where j_o represents for exchange current density, n is active site density, c is elementary charge (1.6×10^{-19} C), and z ($z = 2$) is the transferred electron number per hydrogen molecule. The j_o was obtained by extrapolating the Tafel curves. Subsequently, the TOF of 1T-2H MoS_2 was calculated to be 88 s^{-1}, significantly higher than that of 1T MoS_2 (55 s^{-1}) and 2H MoS_2 (13 s^{-1}) (Fig. 3(c)), indicating the more efficient active sites in the 1T-2H MoS_2 plane.

To further investigate the charge transfer capability of different in-plane active sites in MoS_2, the on-chip electrochemical impedance spectroscopy (EIS) tests were conducted at –200 mV vs. reversible hydrogen electrode (RHE) and the results are shown in Fig. S9 in

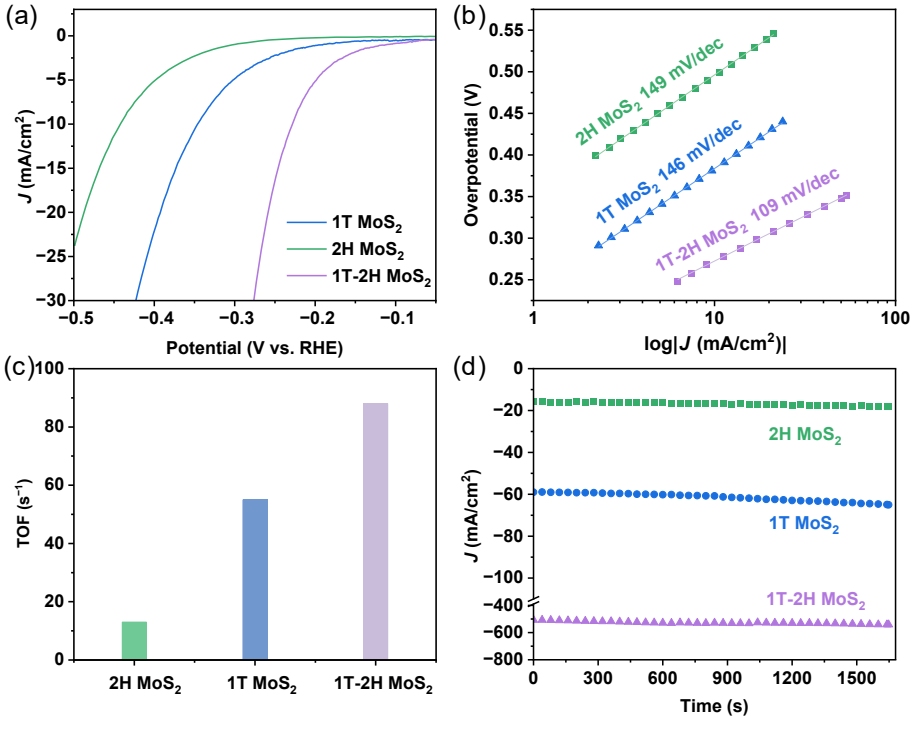

Figure 3 (a) Polarization curves of 2H, 1T, and 1T-2H MoS_2. (b) Corresponding Tafel slopes of samples. (c) The TOF of different MoS_2 sites calculated based on the estimated number of active sites in the selected areas. (d) Chronoamperometric response of samples in a 0.5 M H_2SO_4 electrolyte at –0.45 V vs. RHE.

the ESM. After fitting the data with an equivalent circuit, the charge transfer resistance (R_{ct}) of 1T-2H MoS_2 was found to be only 4320 Ω, significantly lower than that of 2H MoS_2 (24.7 kΩ) and 1T MoS_2 (6082 Ω), indicating a faster charge transfer process. Generally, the catalytic activity of a catalyst is also closely related to its electrochemical surface area (ECSA), which is linearly proportional to the double-layer capacitance (C_{dl}). As shown in Figs. S10(a)–S10(c) in the ESM, we calculated the C_{dl} of different catalysts using cyclic voltammetry (CV) in 0.5 M H_2SO_4. The relationship between scan rate and current density is presented in Fig. S10(d) in the ESM, where the slope of the fitted line represents the C_{dl} value for each catalyst. The C_{dl} value of 1T-2H MoS_2 is approximately 0.33 mF/cm², which is 3 times than that of 1T MoS_2 and 6 times than that of 2H MoS_2. These electrochemical results confirm that the designed and synthesized 1T-2H MoS_2 basal plane has a larger electrochemical surface area in electrocatalysis, thus providing more active sites and leading to superior catalytic performance. Furthermore, the operational stability of different types of active sites was evaluated. Figure 3(d) shows the time-dependent current density curves of different samples under an applied potential of –0.45 V vs. RHE, demonstrating the long-term stability of the 1T-2H MoS_2 heterostructure interface at higher current density. The structural stability of the heterojunction within the exposed window after chronoamperometry testing was characterized using Raman spectra. As shown in Fig. S11 in the ESM, there is no significant degradation of the 1T-2H MoS_2 heterojunction after the electrochemical reaction.

To elucidate the activity origin of the 1T-2H MoS_2 heterostructure, we analyzed its electronic structure and thermodynamic reaction pathways by DFT calculations. Figures 4(a) and 4(b) show the three-dimensional (3D) and 2D charge density difference distribution of a lateral 1T-2H MoS_2 heterostructure. It can be seen that charge redistribution occurs at the 1T-2H MoS_2 interface with electrons transferring from 1T to 2H MoS_2. The amount of transferred charge was determined to be 0.48 e (Fig. 4(c)), thus forming electron-rich 2H MoS_2 and electron-deficient 1T MoS_2. Furthermore, the free-energy profiles of HER on 2H, 1T, and 1T-2H MoS_2 were calculated. Figure S12 in the ESM shows the optimized atomic structure models of 2H and 1T MoS_2. As shown in Fig. 4(d), the Gibbs adsorption free energy of H* is insufficiently weak at the basal plane of 2H MoS_2 and excessively strong at the basal plane of 1T MoS_2. Benefitting from charge redistribution, the interface sites of the heterostructure exhibit significantly lower overpotential than the basal plane of 1T and 2H MoS_2. The interfacial S atom at the top site of 1T MoS_2 ($S1_{T-t}$) presents the smallest overpotential of 0.37 V. Besides, crystal orbital Hamilton population (COHP) analysis was used to determine the chemical bonding of the S–H pair. As depicted in Fig. 4(e), the projected COHP (pCOHP) analysis demonstrates that the antibonding orbitals gradually elevate above the Fermi level in the order of 2H, 1T-2H, and 1T MoS_2, signifying the enhanced bonding strength of the S–H bonds. The bonding strength of the S–H bonds on different structures was further determined by the integrated pCOHP (IpCOHP). Higher IpCOHP signifies greater antibonding state occupation by orbital electrons, indicating more robust interatomic bonding. The moderate IpCOHP of $S1_{T-t}$ reveals its appropriate bonding strength and thus superior HER activity than 2H and 1T MoS_2.

3 Conclusions

In this study, by conducting electrocatalytic tests at the microregion level using OCEMs, we revealed that the well-defined long-range ordered heterojunction of 1T-2H MoS_2, constructed via lithium intercalation, exhibited superior HER activity. The heterojunction shows an overpotential of only 226 mV at a cathodic current density of 10 mA/cm², surpassing that of 1T and 2H MoS_2 (345 mV for 1T MoS_2 and 445 mV for 2H MoS_2). Furthermore, DFT

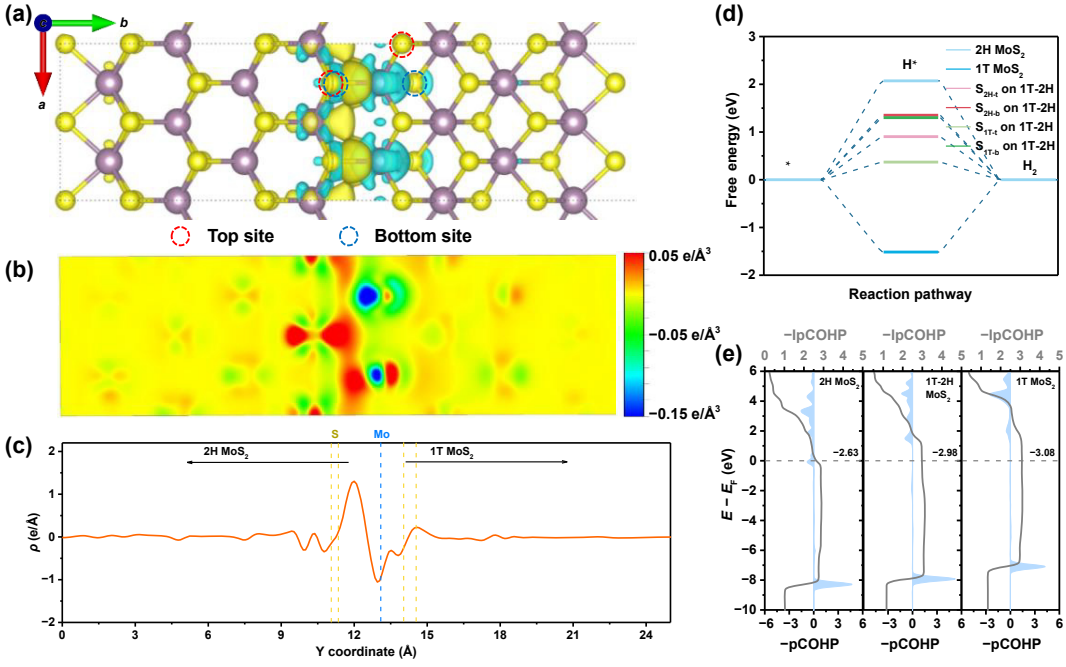

Figure 4 (a) 3D and (b) 2D charge density difference distribution of a lateral 1T-2H MoS_2 heterostructure. Yellow and blue colors in (a) show the positive and negative values of electron quantities, respectively. The isosurface level of (a) is 0.025 e/Å^3. (c) Plane-averaged charge density difference of a lateral 1T-2H MoS_2 heterostructure. (d) Calculated free-energy profiles of HER on 2H, 1T, and 1T-2H MoS_2. (e) pCOHP and IpCOHP of the S–H pair on 2H, 1T-2H, and 1T MoS_2.

calculations demonstrated that the charge redistribution occurs at the 1T-2H MoS_2 interface with electrons transferring from 1T to 2H MoS_2, and the interfacial S atom at the top site of 1T MoS_2 presents the smallest overpotential of 0.37 V. Moreover, the interference from highly active edge sites was avoided by precisely exposing specific active windows, quantitatively revealing the catalytic activity order of different types of MoS_2 active sites. This research enables a systematic investigation of the HER activity at various in-plane active sites in MoS_2. It lays the foundation for quantitatively analyzing activity in other two-dimensional materials.

4 Experimental section

4.1 Materials synthesis

Synthesis of 1T-2H MoS_2: The few-layer MoS_2 nanosheets were obtained through mechanical exfoliation methods. In a typical mechanical exfoliation process, appropriate thin MoS_2 crystals (Shanghai Onway Technology Co., Ltd) were first peeled off from their bulk crystals by using 3M Scotch tape. These freshly cleaved thin crystals on Scotch tape were brought into contact with viscous polydimethylsiloxane (PDMS). After removing the Scotch tape, the few-layered MoS_2 nanosheets remaining on the PDMS were subsequently transferred onto the as-prepared silicon using a precision transfer platform (Metatest E1-G). Then, the silicon was soaked in 2.4 M n-butyl lithium solution for 2 h, and even longer, the 1T-2H MoS_2 and 1T MoS_2 could be obtained.

4.2 Device fabricate

Firstly, the substrate containing 1T-2H MoS_2 was spin-coated with methyl methacrylate (MMA) and PMMA layers. Subsequently, electron-beam lithography (EBL) treatment was performed using a JEOL JSM-IT500 In Touch Scope to create electrode patterns that connected the MoS_2 to the pads. After that, Cr/Au electrodes (5/120 nm) were deposited through thermal evaporation as internal electrodes. A lift-off process using acetone was then carried out to remove the MMA and PMMA layers. The resulting device was once again coated with MMA and PMMA, and EBL was employed to remove MMA and PMMA in the selected basal plane area using a developer mixture of methyl isobutyl ketone (MIBK) and isopropanol (IPA) in a 1:3 ratio.

4.3 Materials characterization

The morphology of MoS_2 nanosheets was examined by optical microscopy (Meta E1-G). The TEM (FEI Tecnai G2 F20 U-TWIN), and AC-HAADF-STEM (probe-corrected JEOL ARM200F with an acceleration voltage of 80 kV) were conducted after the MoS_2 nanosheets were transferred to silicon nitride membrane (CleanSiN). XRD measurements were performed on the Rigaku SmartLab 9 Kw (Cu Kα radiation, λ = 1.54 Å). Raman spectra and photoluminescence (PL) spectra were collected by a spectrometer (WITec Alph300) equipped with a grating of 600 grooves/mm.

4.4 Electrochemical characterization

HER measurements were conducted on an electrochemical workstation (CHI760E) utilizing a three-electrode setup, with a graphite rod serving as the counter electrode and an Ag/AgCl electrode as the reference electrode. The exposed area of the MoS_2 within the electrochemical microcells functioned as the working electrode, and 0.5 M H_2SO_4 was chosen as the electrolyte. Polarization curves were acquired by scanning the potential of the working electrode from 0 to −0.75 V relative to the reference electrode at a scan rate of 5 mV/s. All potentials in this study were referred to the RHE. The current densities were normalized to the exposed area of the MoS_2 flakes.

4.5 Computational methods

DFT calculations with spin-polarization were conducted using the Vienna *ab initio* simulation package (VASP) [37, 38] based on DFT

[39] and the projector-augmented wave (PAW) [40, 41] method. The electronic exchange and correlation effects were described by the Bayesian error estimation exchange-correlation functional with van der Waals interactions (BEEF-vdW) [42]. To ensure the convergence for the total energy, a plane-wave cutoff energy of 450 eV with Fermi-level smearing of 0.05 eV was used. The Brillouin zone was sampled with Monkhorst–Pack k-point meshes of 3 × 1 × 1 for 1T-2H MoS_2 heterostructures. Besides, geometry optimizations were performed until the force of the system converged to 0.02 eV/Å and the energies converged within 10^{-5} eV. The lateral 1T-2H MoS_2 heterostructure was terminated with S monomers and separated from each other by at least 9 Å in the *y*-direction. A 16 Å vacuum layer was set in the *z*-direction to separate the slabs. To gain insights into the local orbital interactions, we conducted a COHP analysis using the LOBSTER 5.0.0 package [43, 44]. To investigate charge transfer between interfaces, the flux charge density difference was determined using the following equation

$$\Delta\rho_{\text{1T-2H MoS}_2} = \rho_{\text{total}} - (\rho_{\text{2H MoS}_2} + \rho_{\text{1T MoS}_2})$$

Electronic Supplementary Material: Supplementary material (experimental section, Raman spectra, XRD results, AFM results, electrocatalytic results, DFT calculation results) is available in the online version of this article at https://doi.org/10.26599/NR.2025.94907020.

Data availability

All data needed to support the conclusions in the paper are presented in the manuscript and the Electronic Supplementary Material. Additional data related to this paper may be requested from the corresponding author upon request.

Acknowledgements

We acknowledge the financial support from the National Key R&D Program of China (Nos. 2021YFA1202802, 2022YFF0712200, and 2022YFE0127400), the National Natural Science Foundation of China (No. 22409037), the Young Elite Scientists Sponsorship Program by BAST (No. BYESS2023410), and the CAS Pioneer Hundred Talents Program.

Declaration of competing interest

All the contributing authors report no conflict of interests in this work.

Author contribution statement

B. W. L: Data curation, project administration, experimental design, validation, and writing manuscript. J. J. X., S. S. X., and X. Y. L.: Data curation, validation, and experimental design. W. Y. Y., S. G. L., Y. T. D., and Q. H. Z.: Data curation and validation. Y. G. and B. W.: Project administration, funding acquisition, and writing manuscript. All the authors have approved the final manuscript.

Use of AI statement

None.

References

[1] Lu, Q. P.; Yu, Y. F.; Ma, Q. L.; Chen, B.; Zhang, H. 2D transition-metal-dichalcogenide-nanosheet-based composites for photocatalytic and electrocatalytic hydrogen evolution reactions. *Adv. Mater.* **2016**, *28*, 1917–1933.

[2] Jin, H. Y.; Guo, C. X.; Liu, X.; Liu, J. L.; Vasileff, A.; Jiao, Y.; Zheng, Y.; Qiao, S. Z. Emerging two-dimensional nanomaterials for electrocatalysis. *Chem. Rev.* **2018**, *118*, 6337–6408.

[3] Chaturvedi, A.; Chen, B.; Zhang, K. K.; He, Q. Y.; Nam, G. H.; You, L.; Lai, Z. C.; Tan, C. L.; Tran, T. H.; Liu, G. G. et al. A universal method for rapid and large-scale growth of layered crystals. *SmartMat* **2020**, *1*, e1011.

[4] Venkateshwaran, S.; Devi, P.; Murugan, P.; Senthil Kumar, S. M. Simple immersion in polar solvents induces targeted 1T phase conversion of MoS_2 for HER: A greener approach. *ACS Appl. Energy Mater.* **2024**, *7*, 1037–1050.

[5] Jaramillo, T. F.; Jørgensen, K. P.; Bonde, J.; Nielsen, J. H.; Horch, S.; Chorkendorff, I. Identification of active edge sites for electrochemical H_2 evolution from MoS_2 nanocatalysts. *Science* **2007**, *317*, 100–102.

[6] Li, G. Q.; Zhang, D.; Qiao, Q.; Yu, Y. F.; Peterson, D.; Zafar, A.; Kumar, R.; Curtarolo, S.; Hunte, F.; Shannon, S. et al. All the catalytic active sites of MoS_2 for hydrogen evolution. *J. Am. Chem. Soc.* **2016**, *138*, 16632–16638.

[7] Chen, B.; Hu, P.; Yang, F.; Hua, X. J.; Yang, F. F.; Zhu, F.; Sun, R. Y.; Hao, K.; Wang, K. S.; Yin, Z. Y. Porousized MoS_2 nano islands enhance HER/OER bifunctional electrocatalysis. *Small* **2023**, *19*, 2207177

[8] Xiong, J. J.; Cai, Y. C.; Dong, W. L.; Luo, X. Y.; Yu, Z. L.; Liu, B. W.; Liu, L. Q.; Liang, T.; Wang, Z. X.; Gao, Y. et al. Strain derived from bubbles at monolayer MoS_2/hBN interfaces for enhanced hydrogen evolution reaction activity. *Chem Catal.* **2024**, *4*, 100951.

[9] Wang, D. G.; Wu, J. X.; Jiao, L. Y.; Xie, L. M. *In situ* identification of active sites during electrocatalytic hydrogen evolution. *Nano Res.* **2023**, *16*, 12910–12918.

[10] Wang, F.; Hao, M.; Liu, W.; Yan, P. J.; Fang, B. Z.; Li, S. J.; Liang, J. S.; Zhu, M. M.; Cui, L. Low-cost fabrication of highly dispersed atomically-thin MoS_2 nanosheets with abundant active Mo-terminated edges. *Nano Mater. Sci.* **2021**, *3*, 205–212.

[11] Zavala, L. A.; Kumar, K.; Martin, V.; Maillard, F.; Maugé, F.; Portier, X.; Oliviero, L.; Dubau, L. Direct evidence of the role of Co or Pt, Co single-atom promoters on the performance of MoS_2 nanoclusters for the hydrogen evolution reaction. *ACS Catal.* **2023**, *13*, 1221–1229.

[12] Chen, J. M.; Lin, Y. P.; Wang, H.; Li, J. M.; Liu, S. J.; Lee, J. M.; Zhao, Q. 2D molybdenum compounds for electrocatalytic energy conversion. *Adv. Funct. Mater.* **2022**, *33*, 2210236.

[13] Tsai, C.; Li, H.; Park, S.; Park, J.; Han, H. S.; Nørskov, J. K.; Zheng, X. L.; Abild-Pedersen, F. Electrochemical generation of sulfur vacancies in the basal plane of MoS_2 for hydrogen evolution. *Nat. Commun.* **2017**, *8*, 15113.

[14] Gan, X. R.; Lee, L. Y. S.; Wong, K. Y.; Lo, T. W.; Ho, K. H.; Lei, D. Y.; Zhao, H. M. 2H/1T phase transition of multilayer MoS_2 by electrochemical incorporation of S vacancies. *ACS Appl. Energy Mater.* **2018**, *1*, 4754–4765

[15] Zhu, Y. R.; Lim, J.; Zhang, Z. P.; Wang, Y.; Sarkar, S.; Ramsden, H.; Li, Y.; Yan, H.; Phuyal, D.; Gauriot, N. et al. Room-temperature photoluminescence mediated by sulfur vacancies in 2D molybdenum disulfide. *ACS Nano* **2023**, *17*, 13545–13553.

[16] Zhou, Y.; Li, C.; Zhang, Y.; Wang, L.; Fan, X. L.; Zou, L. W.; Cai, Z.; Jiang, J. M.; Zhou, S.; Zhang, B. et al. Controllable thermochemical generation of active defects in the horizontal/vertical MoS_2 for enhanced hydrogen evolution. *Adv. Funct. Mater.* **2023**, *33*, 2304302.

[17] Karvonen, L.; Säynätjoki, A.; Huttunen, M. J.; Autere, A.; Amirsolaimani, B.; Li, S. S.; Norwood, R. A.; Peyghambarian, N.; Lipsanen, H.; Eda, G. et al. Rapid visualization of grain boundaries in monolayer MoS_2 by multiphoton microscopy. *Nat. Commun.* **2017**, *8*, 15714.

[18] He, Y. M.; Tang, P. Y.; Hu, Z. L.; He, Q. Y.; Zhu, C.; Wang, L. Q.; Zeng, Q. S.; Golani, P.; Gao, G. H.; Fu, W. et al. Engineering grain boundaries at the 2D limit for the hydrogen evolution reaction. *Nat. Commun.* **2020**, *11*, 57.

[19] Peng, R.; Liang, L. B.; Hood, Z. D.; Boulesbaa, A.; Puretzky, A.; Ievlev, A. V.; Come, J.; Ovchinnikova, O. S.; Wang, H.; Ma, C. et al. In-plane heterojunctions enable multiphasic two-dimensional (2D) MoS_2 nanosheets as efficient photocatalysts for hydrogen evolution from water reduction. *ACS Catal.* **2016**, *6*, 6723–6729.

[20] Nam, G. H.; He, Q. Y.; Wang, X. Z.; Yu, Y. F.; Chen, J. Z.; Zhang, K.; Yang, Z. Z.; Hu, D. Y.; Lai, Z. C.; Li, B. et al. In-plane anisotropic properties of 1T'-MoS_2 layers. *Adv. Mater.* **2019**, *31*, 1807764.

[21] Niu, H.; Zou, Z. G.; Wang, Q.; Zhu, K.; Ye, K.; Wang, G. L.; Cao, D. X.; Yan, J. Structurally stable ultrathin 1T-2H MoS_2 heterostructures coaxially aligned on carbon nanofibers toward superhigh-energy-density supercapacitor and enhanced electrocatalysis. *Chem. Eng. J.* **2020**, *399*, 125672.

[22] Sun, C.; Wang, L. L.; Zhao, W. W.; Xie, L. B.; Wang, J.; Li, J. M.; Li, B. X.; Liu, S. J.; Zhuang, Z. C.; Zhao, Q. Atomic-level design of active site on two-dimensional MoS_2 toward efficient hydrogen evolution: Experiment, theory, and artificial intelligence modelling. *Adv. Funct. Mater.* **2022**, *32*, 2206163.

[23] Wang, W. B.; Qi, J. L.; Wu, Z. X.; Zhai, W.; Pan, Y. H.; Bao, K.; Zhai, L.; Wu, J. K.; Ke, C. X.; Wang, L. Z. et al. On-chip electrocatalytic microdevices. *Nat. Protoc.* **2023**, *18*, 2891–2926.

[24] Zhang, J.; Wu, J. J.; Guo, H.; Chen, W. B.; Yuan, J. T.; Martinez, U.; Gupta, G.; Mohite, A.; Ajayan, P. M.; Lou, J. Unveiling active sites for the hydrogen evolution reaction on monolayer MoS_2. *Adv. Mater.* **2017**, *29*, 1701955.

[25] Yang, H.; Zhao, Y. H.; Wen, Q. L.; Mi, Y.; Liu, Y. W.; Li, H. Q.; Zhai, T. Y. Single $MoTe_2$ sheet electrocatalytic microdevice for *in situ* revealing the activated basal plane sites by vacancies engineering. *Nano Res.* **2021**, *14*, 4814–4821.

[26] Ling, N.; Zheng, S. J.; Lee, Y.; Zhao, M. L.; Kim, E.; Cho, S.; Yang, H. E. J. Active hydrogen evolution on the plasma-treated edges of WTe_2. *APL Mater.* **2021**, *9*, 061108.

[27] Fu, Q.; Han, J. C.; Wang, X. J.; Xu, P.; Yao, T.; Zhong, J.; Zhong, W. W.; Liu, S. W.; Gao, T. L.; Zhang, Z. H. et al. 2D transition metal dichalcogenides: Design, modulation, and challenges in electrocatalysis. *Adv. Mater.* **2021**, *33*, 1907818.

[28] Gao, Y.; Wang, L. D.; Chen, X. Q.; Du, Y.; Wang, B. Revisiting electrocatalyst design by a knowledge graph of Cu-based catalysts for CO_2 reduction. *ACS Catal.* **2023**, *13*, 8525–8534.

[29] Xie, R.; Luo, W. C.; Zou, L. W.; Fan, X. L.; Li, C.; Lv, T. Z.; Jiang, J. M.; Chen, Z. H.; Zhou, Y. Low-temperature synthesis of colloidal few-layer WTe_2 nanostructures for electrochemical hydrogen evolution. *Discover Nano* **2023**, *18*, 44.

[30] Yang, R. J.; Fan, Y. Y.; Mei, L.; Shin, H. S.; Voiry, D.; Lu, Q. Y.; Li, J.; Zeng, Z. Y. Synthesis of atomically thin sheets by the intercalation-based exfoliation of layered materials. *Nat. Synth.* **2023**, *2*, 101–118.

[31] Chhowalla, M.; Liu, Z. F.; Zhang, H. Two-dimensional transition metal dichalcogenide (TMD) nanosheets. *Chem. Soc. Rev.* **2015**, *44*, 2584–2586.

[32] Wu, Y. C.; Wang, J. Y.; Li, Y. B.; Zhou, J. W.; Wang, B. Y.; Yang, A. K.; Wang, L. W.; Hwang, H. Y.; Cui, Y. Observation of an intermediate state during lithium intercalation of twisted bilayer MoS_2. *Nat. Commun.* **2022**, *13*, 3008.

[33] Yu, Y. F.; Nam, G. H.; He, Q. Y.; Wu, X. J.; Zhang, K.; Yang, Z. Z.; Chen, J. Z.; Ma, Q. L.; Zhao, M. T.; Liu, Z. Q. et al. High phase-purity 1T'-MoS_2- and 1T'-$MoSe_2$-layered crystals. *Nat. Chem.* **2018**, *10*, 638–643.

[34] Vedhanarayanan, B.; Shi, J.; Lin, J. Y.; Yun, S. N.; Lin, T. W. Enhanced activity and stability of MoS_2 through enriching 1T-phase by covalent functionalization for energy conversion applications. *Chem. Eng. J.* **2021**, *403*, 126318.

[35] Li, S. W.; Huang, C.; Gao, L.; Shen, Q. Y.; Li, P.; Qu, X. H.; Jiao, L. F.; Liu, Y. C. Unveiling the "proton lubricant" chemistry in aqueous Zinc-MoS_2 batteries. *Angew. Chem., Int. Ed.* **2022**, *61*, e202211478.

[36] Wen, S. D.; Liu, B. W.; Li, W.; Liang, T.; Li, X. L.; Yi, D.; Luo, B.; Zhi, L. J.; Liu, D.; Wang, B. A battery process activated highly efficient carbon catalyst toward oxygen reduction by stabilizing lithium-oxygen bonding. *Adv. Funct. Mater.* **2022**, *32*, 2203960.

[37] Kresse, G.; Hafner, J. *Ab initio* molecular dynamics for liquid metals. *Phys. Rev. B* **1993**, *47*, 558–561.

[38] Kresse, G.; Furthmüller, J. Efficient iterative schemes for *ab initio* total-energy calculations using a plane-wave basis set. *Phys. Rev. B* **1996**, *54*, 11169–11186.

[39] Hohenberg, P.; Kohn, W. Inhomogeneous electron gas. *Phys. Rev.* **1964**, *136*, B864–B871.

[40] Blöchl, P. E. Projector augmented-wave method. *Phys. Rev. B* **1994**, *50*, 17953–17979.

[41] Kresse, G.; Joubert, D. From ultrasoft pseudopotentials to the projector augmented-wave method. *Phys. Rev. B* **1999**, *59*, 1758–1775.

[42] Wellendorff, J.; Lundgaard, K. T.; Møgelhøj, A.; Petzold, V.; Landis, D. D.; Nørskov, J. K.; Bligaard, T.; Jacobsen, K. W. Density functionals for surface science: Exchange-correlation model development with Bayesian error estimation. *Phys. Rev. B* **2012**, *85*, 235149.

[43] Deringer, V. L.; Tchougréeff, A. L.; Dronskowski, R. Crystal orbital Hamilton population (COHP) analysis as projected from plane-wave basis sets. *J. Phys. Chem. A* **2011**, *115*, 5461–5466.

[44] Nelson, R.; Ertural, C.; George, J.; Deringer, V. L.; Hautier, G.; Dronskowski, R. LOBSTER: Local orbital projections, atomic charges, and chemical-bonding analysis from projector-augmented-wave-based density-functional theory. *J. Comput. Chem.* **2020**, *41*, 1931–1940.